Polymer 232 (2021) 124158

Contents lists available at ScienceDirect

Polymer

journal homepage: www.elsevier.com/locate/polymer

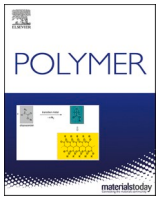

Cavitation in strained polyethylene/nanographene nanocomposites

Vahid Rahmanian, Andrzej Galeski *

Centre of Molecular and Macromolecular Studies, Polish Academy of Sciences, Sienkiewicza 112, 90363, Lodz, Poland

ARTICLE INFO

Keywords:
Polymer nano-composite
Graphene
Cavitation

ABSTRACT

Cavitation in nanocomposites of high-density polyethylene (HDPE) with either graphene nanoplatelets (G) or reduced graphene oxide (rGO) during tensile deformation and impact tests was studied. Composites of HDPE containing 0.1, 0.3, 0.5, and 1 wt% of G (HDPE + G) or rGO (HDPE + rGO) were processed using a twin-screw extruder. Scanning electron microscopy (SEM), small-angle X-ray scattering (SAXS), Izod impact tests, tensile drawing and differential scanning calorimetry (DSC) were used to study HDPE + G and HDPE + rGO nanocomposites. The effects of G and rGO contents on the thermal and mechanical properties of composites were investigated. The inclusion of G platelets in the matrix increased the onset temperature of nonisothermal crystallization of HDPE while inclusions of rGO did not. It was shown that during tensile drawing cavitation occurs in the nanocomposites and HDPE alone. The cavitation pores have sizes above 25 nm with the bias towards larger pores for both types of the nanocomposites. Smaller pores were healed due to the surface tension. In Izod tests the debonding of HDPE from the nanoplatelets occurred ahead of the traveling Izod crack tip giving rise to many voids becoming centers from which fracture emanated radially until impingement. There is only a small difference between HDPE + G and HDPE + rGO nanocomposites: G nanoplatelets nucleate the crystallization of HDPE.

1. Introduction

High-density polyethylene (HDPE) is a flexible synthetic polymer with good mechanical and processing properties. Although HDPE is attractive and low cost, it shows occasional insufficient performances limiting its certain applications. Incorporation of nano-fillers into HDPE is a potential opportunity to counterbalance the properties and its processability. Various nano-reinforcements were already applied for HDPE: calcium carbonate [1], talc [2], silica [3], carbon nanotubes [4,5], organoclay [6,7], various organic nanofibrils [8], cellulose nanocrystals [9], ZnO [10,11], TiO_2 [12,13], Al_2O_3 [14] and graphene e.g. Refs. [15–21]. During tensile deformation, the volume of such nanocomposites increases. Volume increase of nanocomposites usually has two roots: a polymer can debond from inclusions, and a polymer may have a tendency to cavitate itself under extensional stresses. Cavitation inherent to semicrystalline polymers occurs around the yield point while stretching. Inherent cavitation can be controlled and modified by alteration of morphology by changing solidification conditions, e.g. Refs. [22,23]. It was elucidated in the past that cavitation in semicrystalline polymer is triggered by free volume pores that are pertinent to the amorphous phase [24,25]. So, one of the ways of changing cavitation habit is modification of the amorphous phase by various means [26]. For example, alteration of crystalline and amorphous phases of a polymer strongly influences cavitation [27,28]. Most of crystalline polymers are characterized by spherulitic arrangement of crystalline lamellae and the cavitation during stretching differs in different parts of spherulites. The cavitation in spherulites was first studied in details (bulk polyamide 6) long time ago [29]. It was elucidated that equatorial regions of spherulites were particularly susceptible to microvoiding at relatively low draw ratios. At higher draw ratios cavitation occurred at polar regions. It was suggested that extensive chain slip undergoes shear instability and lamellae fragmentation created sites for cavities, all formed in the amorphous phase. The instabilities leading to the lamellae fragmentation were investigated separately [30]. This type of fragmentation concerns the lamellae which are oriented parallel to the tensile direction and is connected with the excessive lamellae thinning and interfacial instabilities but by no means with cavitation. However, cavitation may result from such instabilities as observed and outlined earlier [29]. Under certain tensile deformation conditions, involving positive pressure, the microvoiding mechanism is inoperative, which clearly indicates the main role of the amorphous phase in the triggering and formation of cavities, for example [31]. A

* Corresponding author.
E-mail address: andgal@cbmm.lodz.pl (A. Galeski).

https://doi.org/10.1016/j.polymer.2021.124158
Received 9 May 2021; Received in revised form 1 September 2021; Accepted 3 September 2021
Available online 4 September 2021
0032-3861/

direct evidence of suppression of cavitation by applying hydrostatic pressure was reported for many polymers (polyethylene, polypropylene, polymethylene oxide and others) in a research paper [32]. Hydrostatic pressure of 0.5 kbar was sufficient to prevent for cavitation in all polymers studied. The cavitation related to the stacks of lamellae oriented parallel to the tensile direction at relatively large deformation was recently regarded and named as "large strain cavitation" [33,34].

Crystallinity, crystal thickness, tie-chain concentration, cohesion and consistency of the amorphous phase have been found to be important parameters for cavitation [23]. Additives and nanoadditives can also modify cavitation of a polymer due to stretching by debonding, e.g. Refs. [35–37]. Micro or nano-sized voids can be formed during stretching of nanocomposites containing nanofiller. Debonding of polymer-inclusion relies on the strength of interfacial adhesion and surface tension of a filler and a polymer [38–40].

Filler particles originate intensive shear and stress zones during stretching due to different Young moduli of components. They are located in polar zones and cause initial debonding of matrix-particle and form micro or nanovoids. Micro and nanovoids do not transmit the stress causing the stress concentrations in equatorial zones and their plastic deformation. Initiation, growing and enlarging of voids in the stretching direction leads to whitening [36,41–45]. Debonding of particles from polymer leads to the load transfer from filler to matrix and causes the energy absorption during deformation. Such phenomena enhances the toughness of composites [46]. Before debonding the stress transfer to inclusions depends on their size, shape, surface properties and modulus of particles as well as on interaction of filler-polymer [35,47,48]. After debonding mechanical response of a nanocomposite relies on the properties of a polymer and on complicated pattern of freshly formed cavities. Depending on the type of filler, other attributes of a composite can also be affected: thermal resistivity, electrical, barrier properties and solidification [49].

Mechanisms of cavitation and debonding in crystalline polymers and their composites with inorganic fillers under uni/biaxial tensile stress, were subjects of intensive studies in the past [50,51]. Morphology observations revealed that cavities have sizes in the broad range from nanometers to micrometers. They can be detected; nanometer cavities using small-angle X-ray scattering (SAXS) or larger by light scattering (whitening) [52–54]. Cavitation in semicrystalline polymers is usually initiated at or around the mechanical yielding; hence, the modification of polymer morphology by changing melt solidification or using nano-additives can dramatically change the cavitation [55–57].

A quantitative method to determine stress-induced cavitation is the measurements of the volume increase during stretching [58–60]. The volume increase at the moment of initiation of cavitation is relatively small, which makes it hard to find the accurate onset of cavitation. However, the SAXS technique is very sensitive to nanosized cavities and can be used to find the very beginning of cavitation [15,23].

In this article, we investigated nanocomposites of high density polyethylene (HDPE) with graphene (G) and with reduced graphene oxide (rGO), deformed at room temperature. These conditions support cavitation of plain HDPE as it is known from other studies, e.g. Ref. [61]. Graphene (G) and reduced graphene oxide (rGO) are plate-like nanomaterials differing in interfacial tension towards polyethylene. Hence, one of the aims of the studies will be observing the debonding of plate-like nano-fillers from HDPE.

2. Experimental section

Materials. High-density polyethylene (Hostalen GC 7260) with a melt flow index of 8 g/10 min was purchased from LyondellBasell Corp. Acquired batch of the material was characterized by zero-shear viscosity of 2500 Pa·s at 150 °C (rheometer ARES LS2, TA Instruments). Graphene nanoplatelets with 99.9% purity and 5 nm thickness and reduced graphene oxide (rGO) with 99.9% purity and 0.5–2 nm thickness were purchased from Nanografi, Germany. The reduced graphene oxide was prepared by deoxygenation of graphene oxide.

Sample Preparation. All the materials were dried for 8 h at 70 °C under a vacuum before intense melt compounding. A laboratory co-rotating twin-screw mini-extruder (with a 5 ml cavity) was used to carry out the melt blending at a constant temperature setting of 180 °C along the extruder. In order to minimize the nanofiller aggregation, the HDPE/Graphene and rGO nanocomposites were prepared from masterbatches of HDPE/Graphene and HDPE/rGO containing 1 wt% of nanoparticles by diluting with neat HDPE. All master batches and composites were prepared by compounding for 3 min at 60 rpm and followed for 7 min at 100 rpm. The nanocomposites were prepared with the following graphene concentrations or rGO: 0.1, 0.3, 0.5, and 1%. Neat HDPE was treated in the same way. The samples for further studies were molded at 180 °C for 3min and subsequently cooled in a press with iced-water jackets and held for 5 min. Such method allowed for preparation of nanocomposites with finer crystalline morphology compared to air cooling procedures and, therefore, different cavitation ability.

Mechanical Properties. Tensile drawing of nanocomposites was performed using Instron-5582 Universal Testing Machine in a load range of 0–2 kN. At least five specimens shaped according to EN ISO 527–2 with the length of 80 mm, width of 5 mm, thickness of 1.0 ± 0.1 mm and the gauge length of 50 mm were tested at room temperature of 23 °C at the rate 5%/min. The final results were the average from all 5 samples. The actual shape and sizes of samples during deformation was recorded every 0.5 min by Nikon D50 digital camera in order to determine the local strain and volume strain. The local and volume strains were determined in the same way as reported in the other researches [55,58,62] by dots marked along the entire gauge length at 1 mm distance from each other. The local strain was calculated as a relative change in distance between the markers while the volume strain for local strains was determined as the volume increase of the portion of the material between dots. The sample's thickness was monitored via a small mirror to direct the side shape of the sample to the camera. The thickness of the photographed samples and the distance between markers was used to determine the volume of the samples. The stretching was stopped at selected local strains and samples were fixed in a specially designed frame in order to maintain the strain of a sample for further x-ray studies.

The Izod impact strength of samples was determined with CEAST Resil 5.5 apparatus according to ISO 180. The hammer struck notched specimens with a speed of 3.46 m/s and potential energy of 5.5 J. Samples having dimensions of 64 mm (length) × 10 mm (width) × 4 mm (thickness) were shaped by machining from 4 mm thick plates. Notches were prepared in accordance with ISO 2818 with a manual notch maker at the middle of their length on the 4 mm thick walls. Izod impact tests were performed at ambient temperature for a set of five samples for each material. Izod fracture surfaces were observed in the scanning electron microscope.

Thermal Properties. 6–9 mg samples were encapsuled in aluminum pans and examined during heating and cooling at a constant rate of 10 C°/min under nitrogen flow in a DSC apparatus (TA Q20, Thermal Analysis). Peak melting and peak crystallization temperatures as well as a degree of crystallinity of nanocomposites and HDPE were determined. The heat of fusion of HDPE crystals of 293 J/cm^3 was assumed [63].

Scanning Electron Microscopy. The structure of surfaces uncovered during the Izod impact fracture was studied using SEM JEOL 6010LA (JEOL, Japan) in high-vacuum mode at 20 kV. Surfaces of samples were coated with a 10 nm gold layer by ion sputtering.

Transmission Electron Microscopy. Transmission electron microscopy (TEM) was performed using a TESLA BS500 electron microscope operating at 90 kV. Samples, in the form of approx. 60 nm thick sections, were prepared by cryo-ultrasectioning with an ultramicrotome (PowerTome PC, Boeckeler, USA) with a diamond knife (Diatome, Switzerland). In the case of HDPE/graphene systems, no staining or any other chemical treatment was applied to sections prior to observation.

Small-angle x-ray scattering (SAXS). SAXS was used to determine

structural changes of the samples. A 1.2 m long pin-hole SAXS camera was aligned to GeniX Xenocs X-ray source (Cu K_α, wavelength 0.154 nm, operating at 50 kV and 1 mA). The scattered radiation was collected by Pilatus 100 K detector of the 172 × 172 μm^2 precission (Dectris, Switzerland) allowing for up to 80 nm resolution of scattering objects. The tensile samples were stretched on Instron 5582 Machine until desired local strains were reached and fixed in their stretched state using specially designed clamps before transferring to the SAXS machine. Specimens were stretched to 10, 30, 50, 70, 100 and 200% of local strain. Structural changes of the nanocomposites due to deformation and detection of nanovoids as well as the beginning of the formation of nanovoids were sought.

3. Results and discussion

In Fig. 1a and b the SEM micrographs of graphene and reduced graphene oxide powder are presented. The flat dimensions of grains are roughly around 1 μm for graphene and 10 μm for reduced graphene oxide.

Their real dimensions and thickness can be extimated from SEM micrographs with difficulties. For that purpose we applied small angle x-ray scattering and determination electron density correlation function. A one-dimensional correlation function, K(z), is used in order to obtain detailed information regarding structural parameters such as the average thickness pertaining to the periodic domain structure [64]. The scattering vector q is defined as:

$$q = 4\pi \sin(\Theta)/\lambda \tag{1}$$

while electron density correlation function is defined as:

$$K(z) = \int_0^\infty I(q)\cos(zq)dq \Big/ \int_0^\infty I(q)dq \tag{2}$$

where $I(q)$ is the x-ray scattered intensity, λ is the x-ray wavelength, Θ is the scattering angle while z represents distance/dimension in real space. $K(z)$ is derived from the Fourier transformation of the overall SAXS curve according to eq. (2). This theoretical treatment when applied for the lamellae stacks (as graphene multilayers) requires that the $K(z)$ be based on unoriented samples, where the lamellae structure is isotropically distributed. From the general principles of diffraction theory it follows that the Fourier transformation of the SAXS data (eq. (2)) describes the distribution of the scattered x-ray intensity in reciprocal space and leads to a measurement of real space features due to convoluted staggering of the electron density variations arising from each diffracting object. The integration range is usually limited from q corresponding to the resolution of the SAXS equipment (80 nm in our case) to the value of $4\pi/\lambda$.

The SAXS scattering images and respective electron density correlation functions are depicted in Fig. 2a and b. The 2D SAXS images are isotropic indicating that the powder samples prepared by soft squizing have no anisotropy and the Porod's approach can be applied. The characteristic dimensions were determined from the shapes of correlation functions and are also marked on the plots in Fig. 2a and b. These dimensions can be ascribed to the thickness of graphene and graphene

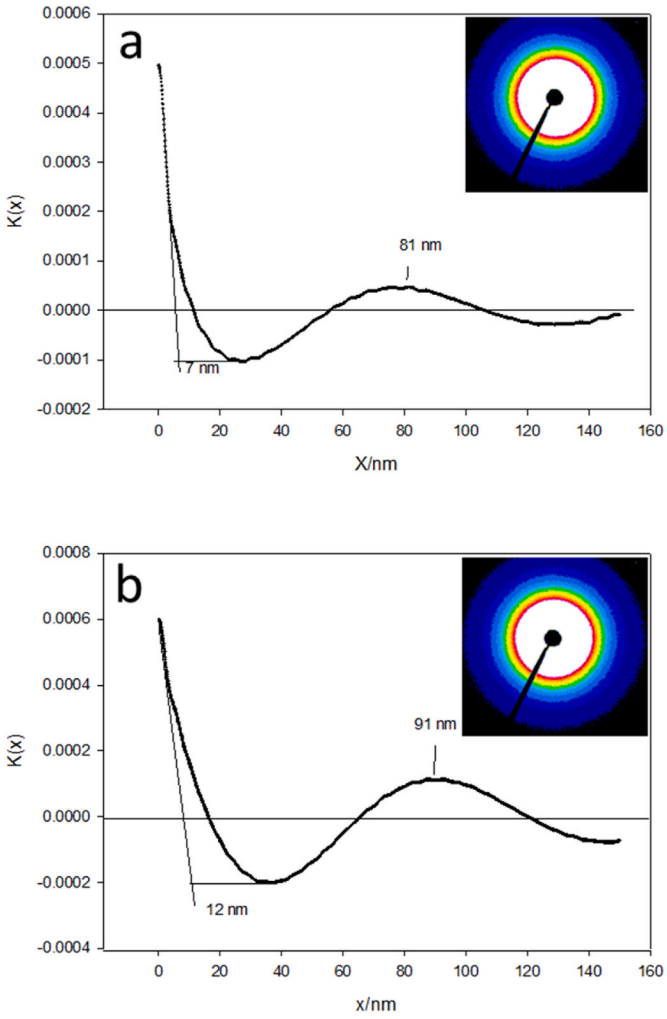

Fig. 2. Electron density correlation functions for powder form of graphene a.) and reduced graphene oxide b.). Original SAXS patterns are placed in the corner of the plots. Characteristic dimensions determined from correlation functions are depicted on the plots. Integration according to eq. (2) beyond the resolution of the SAXS equipment (80 nm) is often regarded as a prediction.

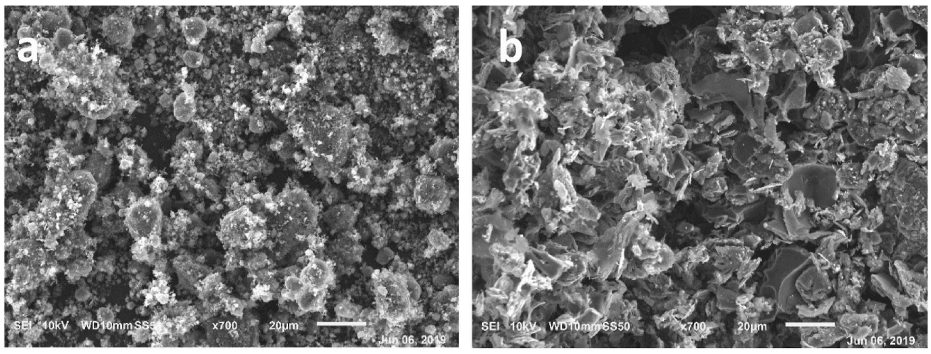

Fig. 1. SEM micrograph of graphene nanoparticles. a.) graphene and b.) reduced graphene oxide.

oxide layers: the average thickness of the platelets is around 7 nm for graphene and 12 nm for reduced graphene oxide, while the lateral dimensions were determined from SEM micrographs from Fig. 1 to be 1 μm and 10 μm for graphene and graphene oxide, respectively. These numbers are significantly different than those claimed by the producer: graphene 5 nm thick and graphene oxide 0.5–2 nm thick. However, it must be remembered that correlation function from SAXS patterns delivers the average value with preference for larger objects, because the scattering intensity depends on the volume of scattering objects. Even a precise direct measurements of graphene layer thickness by AFM is subjected to many restrictions [65]. A graphene monolayer can be considered as having the thickness of only one carbon atom. Its van der Waals radius is 0.170 nm [66] so, graphene and rGO platelets used here are much thicker.

Crystallization of HDPE/graphene nanocomposites was followed by detecting heat flow in DSC apparatus during cooling. The recorded exotherms are presented in Fig. 3. It is evident that graphene platelets influence the crystallization of HDPE. The action of platelets is acceleration of nucleation which resulted in a shift of crystallization onset and crystallization peak toward higher temperature as the concentration of graphene increases and as it is evidenced in Table 1.

Subsequent melting is giving the information on lamellar crystal

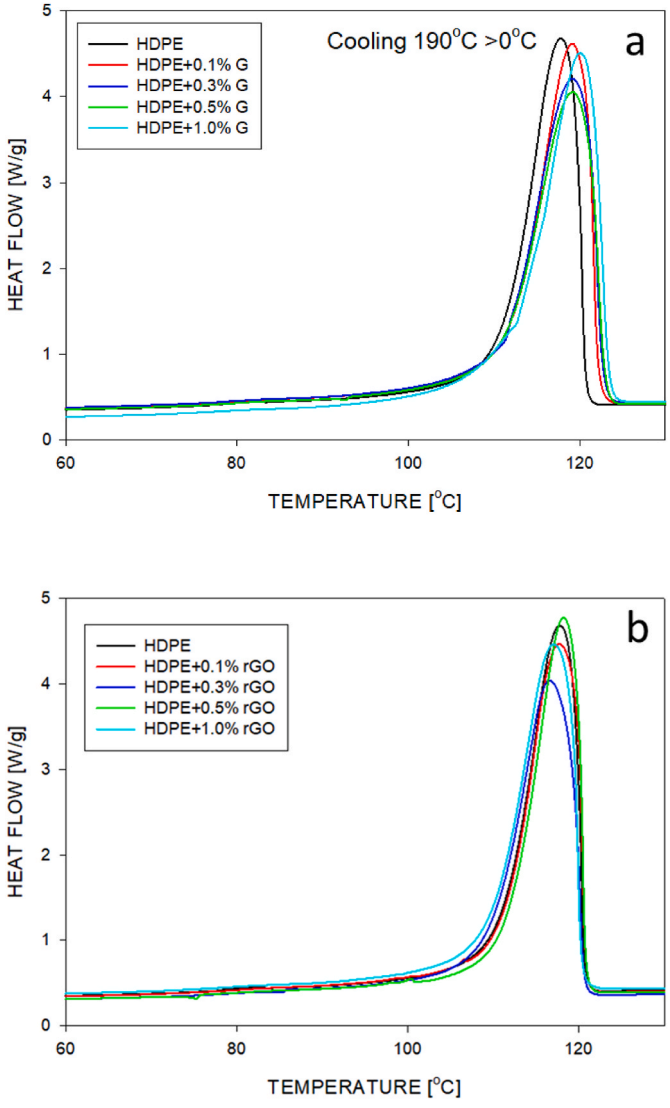

Fig. 3. Exotherms of solidification of a.) HDPE/G and b.) HDPE/rGO nanocomposites during cooling from the melt with the rate of 10 deg/min.

Table 1
Nonisothermal crystallization of HDPE and HDPE + G nanocomposites from melt, cooling from 190 °C with the rate 10 deg/min.

Sample	Crystallization onset [°C]	Crystallization peak [°C]
HDPE	121.5	117.7
HDPE+0.1% G	123.3	119.1
HDPE+0.3% G	123.6	119.3
HDPE+0.5% G	123.7	119.4
HDPE+1.0% G	124.2	120.0

thickness when applying Gibbs-Thompson approach. In principle, the melting data can be converted to the crystal thickness. The Gibbs–-Thomson equation exhibits the depression of the melting temperature of crystals caused by the domination of surface energy over volume energy [67]:

$$T_m(l) \cong T_m^o[1 - 2\sigma_e / \Delta h l] \tag{3}$$

or

$$l = \frac{2\sigma_e T_m^o}{\Delta h\left(T_m^o - T_m\right)} \tag{4}$$

where $\boldsymbol{\sigma_e}$ is the basal surface free energy, and $\boldsymbol{\Delta h}$ is the heat of melting [68]. This form of Gibbs-Thomson equation is derived based on the assumption that the lateral size of lamellae is much larger than their thickness so, the basal planes of lamellae are of importance. For an infinitely thick crystals the formula yields the value of equilibrium melting temperature, $\boldsymbol{T_m^o}$ [69–72]. On the other hand the DSC melting data can be used to determine the crystal thickness based on the melting temperature. Routinely, a crystal thickness is determined based on eq. (5) substituting the measured peak melting temperature, T_m. The obtained value is regarded as the average thickness being a coarse but usuful approximation. The average thickness calculated in this way for the studied polyethylene and nanocomposites were for example: HDPE and HDPE+1% G: $l_c' = 22.9$ nm and 25.3 nm, respectively. However, since the melting occurs over a range of temperature the determination of proper thicknesses requires more refined method. The transformation of DSC melting heat flow (melting enthalpy spreading) to the distribution of crystal thickness, G(l), was derived first by Crist and Mirabella [73] as:

$$G(l) = KP(T)\left(T_m^o - T\right)^2 \tag{5}$$

where K is the normalization constant and $P(T)$ is the DSC melting enthalpy flow.

From Fig. 4 it is evident that the peak of the thickness distribution (around 18–19 nm for all HDPE/G nanocomposites) is significantly lower than the mean crystal thickness determined from DSC peak temperature of crystallization (between 22.9 and 25.3 nm). It is also seen that a shoulder on the right arm of the distribution curve develops for nanocomposites with the increasing content of G indicating the appearance of HDPE lamellar crystals with larger thickness. It is apparently connected with the onset of crystallization at higher temperature for G containing composites as outlined in Fig. 3a and Table 1. Those crystals were nucleated at higher temperature during cooling, hence, were growing for longer time and at slightly higher temperature.

In contrast, the nanocomposites containing rGO do show similar onset of crystallization during cooling and the solidification exotherms are very similar for HDPE and all HDPE + rGO nanocomposites studied (see Fig. 3b). In Fig. 5 the HDPE crystal thickness distribution in 1.0 wt% of rGO nanocomposite is compared with crystals in plain HDPE. Both distributions are very similar indicating very weak nucleating aptitude of rGO towards crystallization of HDPE.

The stress-strain plots in Fig. 6a and b illustrate deformation behavior of all HDPE + G and HDPE + rGO materials with tensile yielding, necking and further plastic flow. The yielding stress is the

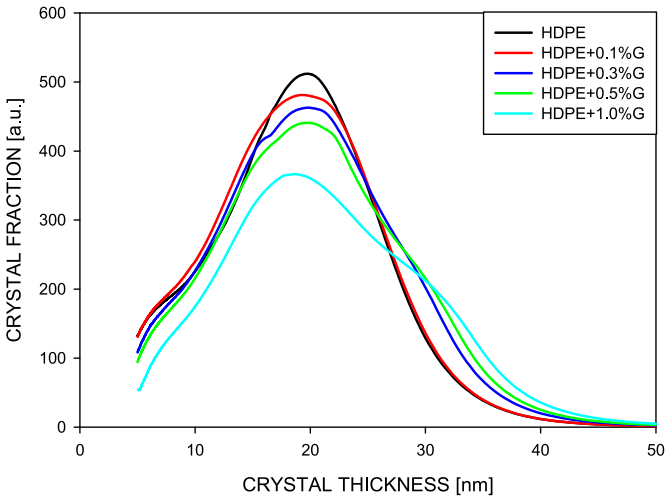

Fig. 4. Distributions of lamellar crystal thickness of HDPE + G nanocomposites. The following data for polyethylene crystals were assumed in calculations: $\sigma_e = 9*10^{-6}$ J/cm^2 [74], $\Delta h_f = 293$ J/cm^3 [75], $T_m^o = 145.1$ °C [72].

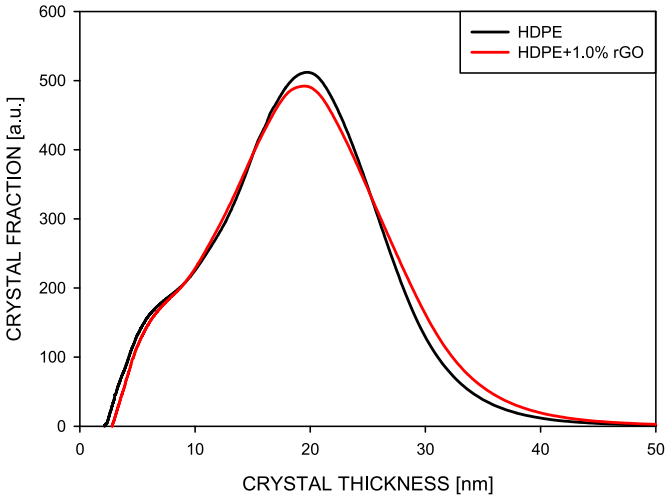

Fig. 5. Distribution of lamellar crystal thickness of HDPE+1.0 wt% reduced graphene oxide nanocomposite. Crystal thickness distribution for plain HDPE is also depicted. The following data for polyethylene crystals were assumed in calculations: $\sigma_e = 9*10^{-6}$ J/cm^2 [74], $\Delta h_f = 293$ J/cm^3 [75], $T_m^o = 145.1$ °C [72].

lowest for plain HDPE, increases with addition of 0.1% of graphene nanofiller and slowly increases with further increase of nanofiller concentration.

The yield stress increase for low content of graphene is connected with concentration of stresses around filler platelets, especiałły those oriented along the drawing direction. However, the yield stress increase with increasing concentration of G is not monotonic and varies from sample to sample. The reason is high sensitivity of the necking to heat generation during plastic drawing, especially just beyond the yield. It is explained in more details based on Fig. 7 where the isothermal condition was enforced by air flow. When the graphene content increased up to 1.0%, the yield stresses are maintained at the level of ≈22 MPa. The reason is due to the overlapping the stress concentration zones around graphenes platelets as they become closer at higher concentrations. At stress concentration zones the yielding becomes easier, at lower applied stress. However, the increase in the crystal thickness due to nucleating activity of graphene causes the yield stress to increase and it must also be accounted.

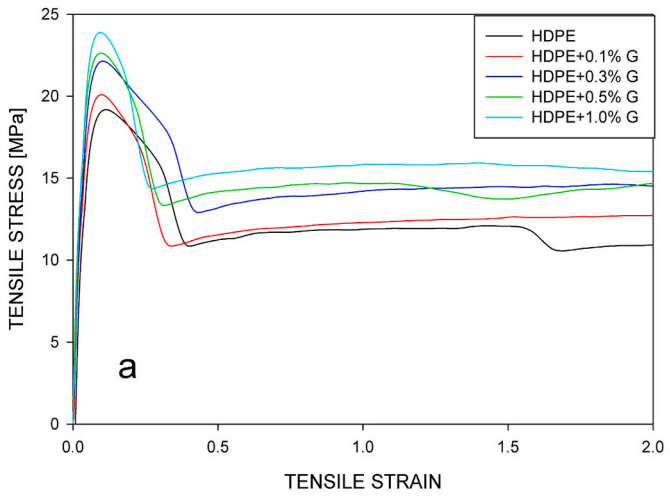

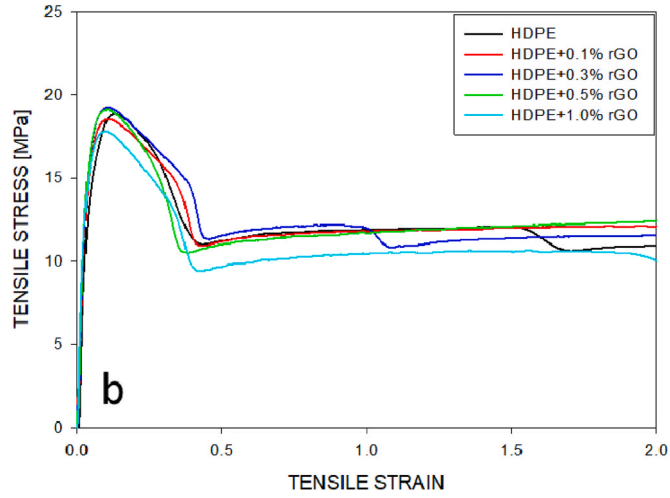

Fig. 6. Exemplary engineering stress-strain plots of HDPE + G (a) and HDPE + rGO (b) nanocomposites. Tensile deformation rate 5%/min at 23 °C. Concentration of nanoparticles are given in the legend on the graphs.

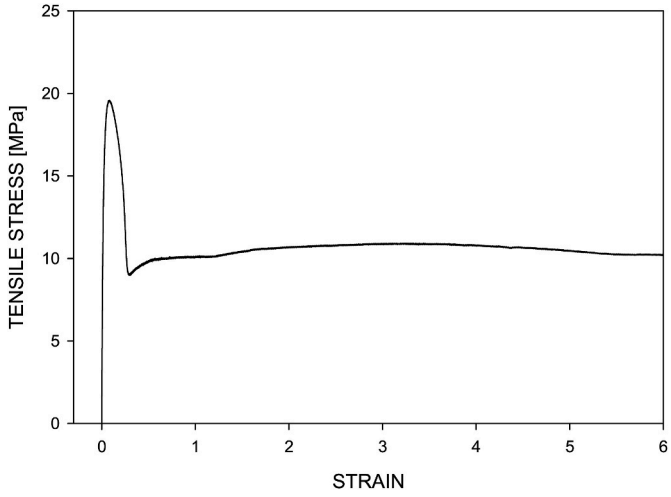

Fig. 7. Exemplary tensile drawing of HDPE + rGO at concentration of 0.5% at nearly isothermal condition enforced by air flow at room temperature.

The yield stress of nanocomposites with reduced graphene oxide behaves differently: it is nearly at the level of plain HDPE independent of rGO concentration. The platelets of rGO are significantly less numerous than the platelets of graphene as it follows from the material characteristics and also from the estimation of average number of graphene or rGO layers in platelets as determined by SAXS and described in Fig. 2a and b. At the same weight concentration the number of rGO platelets are several times lower than the number of graphene platelets. In addition rGO platelets do not induce accelerated crystallization of HDPE.

During drawing the flow stress beyond the yield fluctuates when the region of intense plastic deformation transfers from one end to another in the neck zone. It is a complicated interplay with strengthening due to orientation and local heat generation during drawing. As a result the intense plastic deformation zone changes its position, both ends of the neck are deformed or even another neck is formed at the gauge section of a sample. Environmental chamber of tensile testing equipments usually does not ensure full isothermal condition because of sample thickness (1 mm thick) and its low thermal conductivity (0.2–0.3 W/m/K). The role of heat subtraction is illustrated in Fig. 7 where the tensile drawing of exemplary nanocomposite of HDPE+0.5% of reduced graphnene oxide is presented in nearly isothermal condition. The isothermal condition was enforced by air blowing with the fan at the same room temperature.

It is known from our earlier studies [23,59,61] that tensile drawing of unmodified HDPE involves a significant volume increase (up to 40%), resulting from cavities originated in the amorphous layers between lamellae. Modification of the material by adding nanofiller increases the intensity of cavitation causing an additional volume strain. Such effect is documented in Fig. 8a and b where the volume strain during stretching of HDPE + Graphene and HDPE + rGO nanocomposites are presented. The volume strain amplifies with an increase in nanoparticle content. The samples with higher content of nanoparticles show volume increase up to 60%.

Nanofiller plattlets form stress concentration spots, which can facilitate the formation of additional cavities. Modification of graphene platelets by oxidation followed by reduction does not significantly changes the resulting maximum volume strain, all are slightly below 60%.

Nonhomogeneous deformation observed in plastic flow caused by interplay between strain hardening and softening due to heat generation: resulting volume strain strongly fluctuates. The volume strain data presented in Fig. 8a and b are in the vast part based on measurements of the width, thickness and local strain of those fragment of a sample being nonhomogeneously deformed. Nonetheless, volume strain is undoubtedly increasing with increasing local strain and it is also increasing significantly with increasing concentration of graphene and also with increasing concentration of rGO.

Mechanical properties and the course of tensile deformation of nanocomposites are affected by the properties of a polymer and debonding of polymer materials from nanofillers. The yield stress of a neat polymer is always more considerable for samples with thicker crystals. In composites and nanocomposites the yield stress changes depending on filler or nanofiller effect on mechanical properties that can be either toughening or strengthening. Impact deformation of such materials is directly related to toughening or strengthening effects of nanofiller. Izod impact strength data for nanocomposites of HDPE with G and rGO are collected in Table 2.

It is evident from Table 2 that both nanofillers have moderate negative effect on impact strength of HDPE nanocomposites. The increase of nano-particle content leads to more defects in the structure leading to approx. 20% decrease of Izod Impact strength. The reason of the decrease can be detected in SEM images of fracture surfaces in Fig. 9a, b and c.

Whereas the fracture in plain HDPE is rather brittle (see Fig. 9c), without significant plastic deformation at the surface of cracking path, the fracture of nanocomposites containing G and rGO is completely different (Fig. 9a and b). Evidently the fracture is initiated ahead of

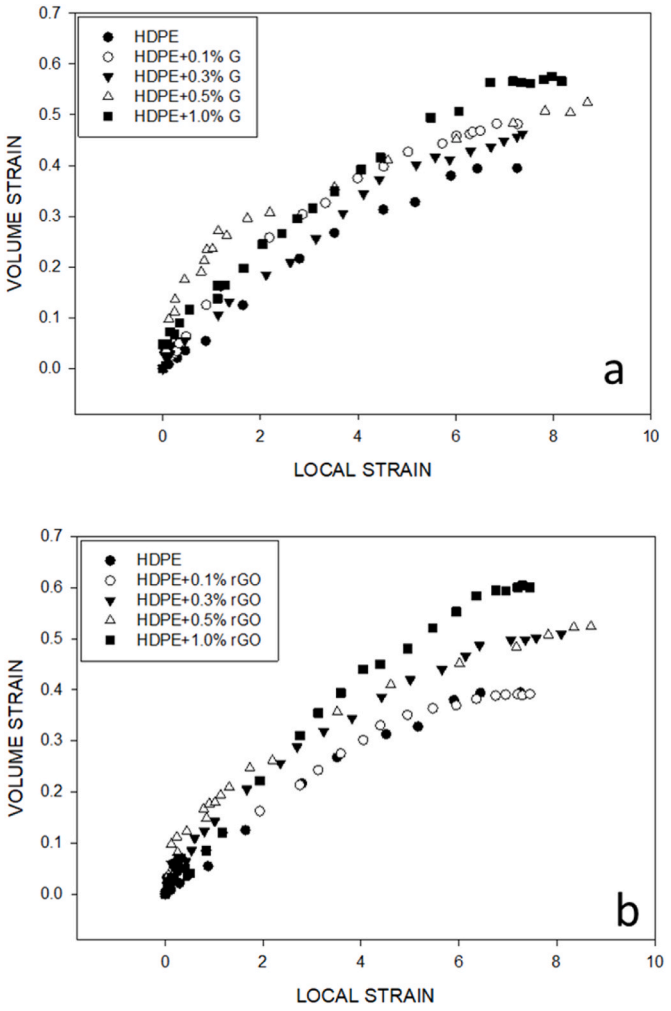

Fig. 8. Volume strain of HDPE + G (a) and HDPE + rGO (b) resulting from tensile deformation. Samples prepared and deformed as shown in Fig. 6a and b.

Table 2
Izod impact properties of nanocomposite samples.

Concentration %	HDPE + G Izod Impact Strenght J/m^2	HDPE + rGO Izod Impact Strenght J/m^2
0.0	24.3 ± 0.8	24.3 ± 0.8
0.1	24.1 ± 0.9	24.5 ± 0.8
0.3	19.6 ± 1.2	21.1 ± 0.9
0.5	18.1 ± 0.9	19.1 ± 1.3
1.0	20.1 ± 0.7	18.8 ± 0.9

traveling crack, in the bulk of the sample, by debonding of a polymer from platelets of graphene and rGO. The voids become the centers around which fracture emanate radially. Examination of images in Fig. 9a and b indicates also that in the centers of each ring there are G or rGO particle lying flat. As the result of debonding many deformation rings, flat and expanding, participate in the fracture.

There is a difference in the course of fracture close to the notch for G and rGO nanocomposites: for G nanocomposites the deforming rings close to the notch do not have evidently possibilities to develop large symmetric ring because the fracture speed is the highest at the beginning, hence they assume hyperbolic structures directed towards the direction of crack propagation (see Fig. 10a). The fracture of rGO nanocomposites undergoes differently at the zone close to notch: the deforming rings apparently have the possibility to develop fully into

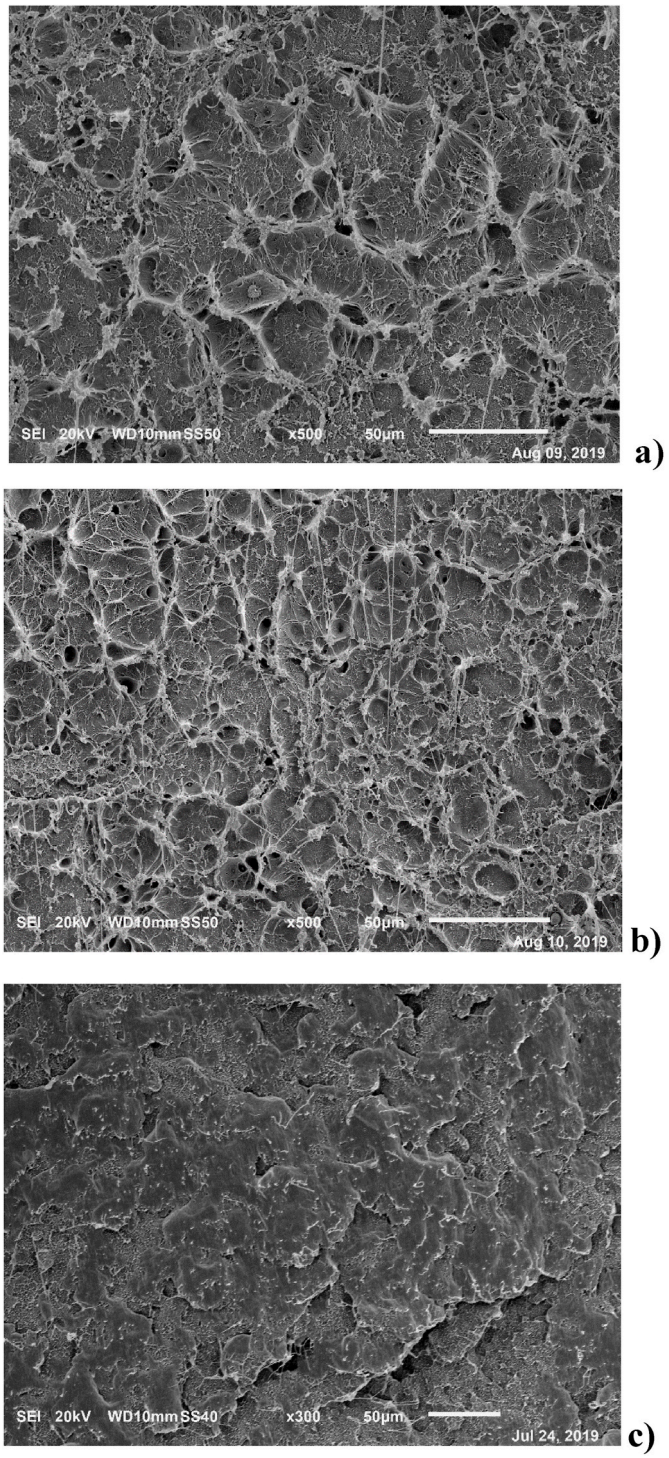

Fig. 9. SEM micrographs of fracture surfaces, focused at some distance from the notch in Izod impact tests: a) HDPE+0.1% G, b) HDPE+0.1% rGO, c) plain HDPE.

circular structures and even impinging with neighbours (Fig. 10b). Farther from the notch the impact fracture of both nanocomposites undergoes with lower rate and with well developed rings, as demonstrated in Fig. 9a and b, all rings are originating from centrally lying nanoplatlets in the plane of fracture. The deformation rings have no correlation with HDPE spherulitic structure, HDPE spherulites having from 40 to 60 µm in diameter independent of nanofiller type and concentration while the rings sizes depend on the position with respect to notch and regardless of the type of nanofiller.

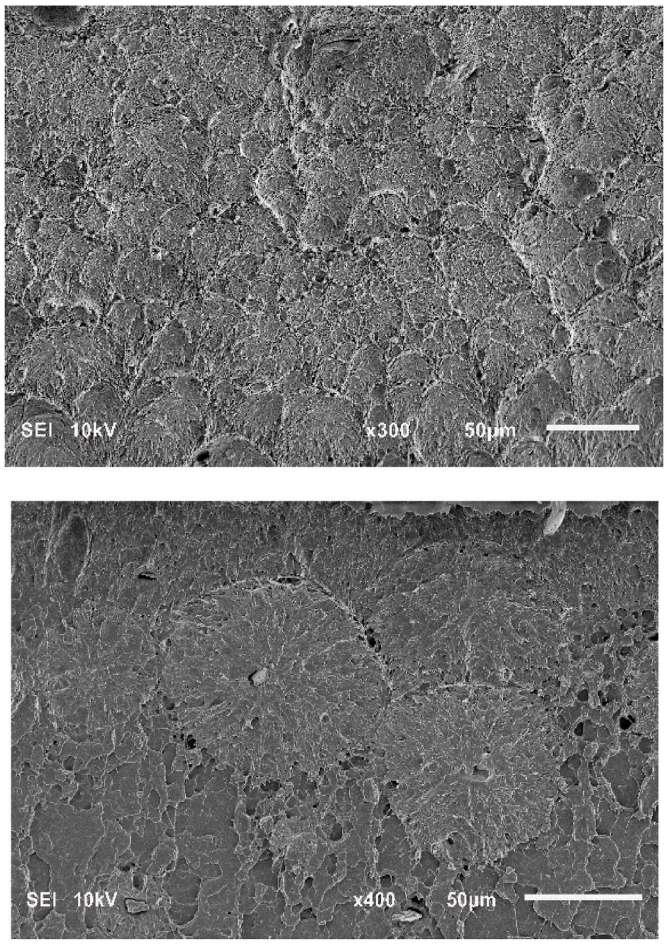

Fig. 10. SEM images of the fracture paths just below the notch, HDPE+0.3% G (a) and HDPE+0.1% rGO (b). Notches are right at the top of images.

The platelets of nanofillers are dispersed in HDPE in a way that no vacancies are between platelets and polymer bulk. The illustration of lack of vacancies are presented in Fig. 11 where the TEM image of a G platelet is surrounded by the polymer bulk. Although the platelet is large, tilted and folded no vacancies can be distinguished in the image.

The modification of usual cavitation accompanying tensile drawing by graphene nanoplatelets was undertaken by in-situ SAXS measurements. Due to larger difference in the electron density X-ray scattering is much stronger from cavities than from the crystal-amorphous elements of the material. Therefore SAXS is a handy tool for elucidation of cavitation of a material. Fig. 12 presents schematic evolution of the SAXS patterns with increasing strain.

SAXS patterns are composed of the scattering from internal structure of a polymer, in the case of HDPE it is scattering from lamellar packing with the characterising dimension being a thickness of lamellae with adhering amorphous layer. It is usually called “long period” and it is related to the electron density difference between HDPE crystals (≈1.0 g/cm^3) and HDPE amorphous phase (≈0.855 g/cm^3). In the case of HDPE used in this study the “long period” scattering is situated at outher ring at a scattering angle corresponding roughly to 30–35 nm. The center of SAXS image for undeformed HDPE is occupied with the beam stop only. For nanocomposites there is a low intensity scattering from G or rGO platelets because of their low concentrations and it is located inside the “long period” outer ring because of their large lateral sizes. As we apply tensile deformation until yielding and beyond, either to HDPE or its nanocomposites, drastic changes occur to SAXS patterns. The outer ring deforms because crystalline lamellae deform and assume enforced orientation while in the inner part of SAXS pattern an intense scattering

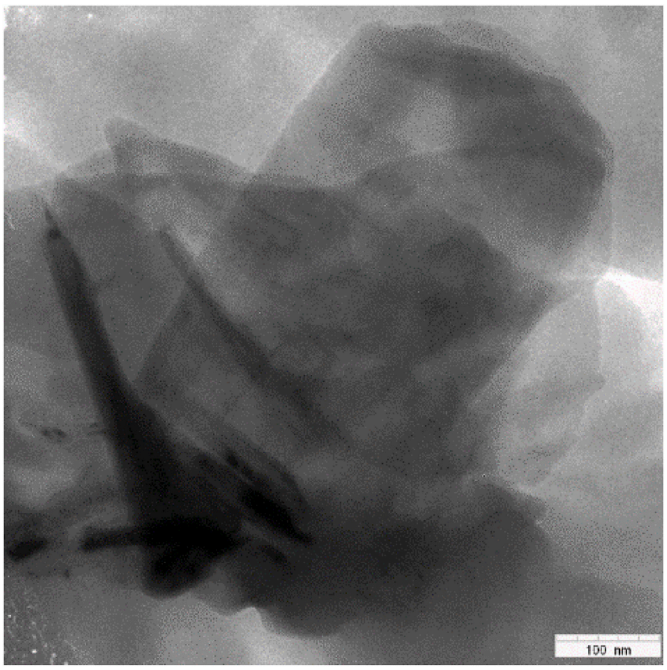

Fig. 11. Exemplary TEM micrograph of ultrathin cryo-section of HDPE+1.0% of graphene nanocomposite. Extensive tilted and folded G layer in the HDPE matrix tightly surrounded by HDPE is seen.

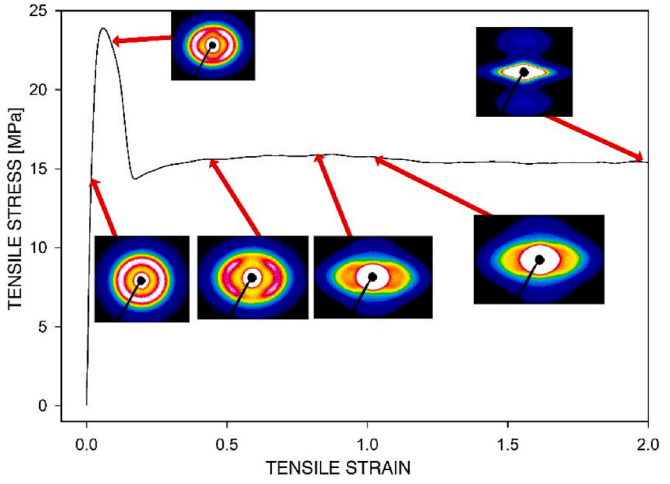

Fig. 12. Schematic evolution of SAXS pattern during tensile deformation of the HDPE + graphene sample. Deformation direction vertical.

appear. It is evidently the scattering by objects with very high electron density difference. We identified them as cavities that appear as the result of tensile deformation. The intensity of scattering is illustrated in Fig. 13 where the Θ scans in the direction perpendicular to tensile direction of SAXS images are presented for HDPE+1% G sample deformed to 0.1 and to 0.7 local strain.

The scattering from lamellae packing is visible at $S^2 \approx 0.005$ for the sample deformed before the yield and no cavities are recorded yet whereas for the sample deformed to local strain of 0.7 a strong scattering from cavities is apparent at low values of S^2 which correspond to large scattering objects. The scattering from lamellae packing has moved to higher values of S^2 indicating its deformation. The characteristic parameter of lamellae packing, long period (*LP*), is determined from the position of peak intensity from one-dimensional sections (background and Lorentz corrected) of 2-D patterns using Bragg's law: $LP = \lambda/2 \sin \Theta$.

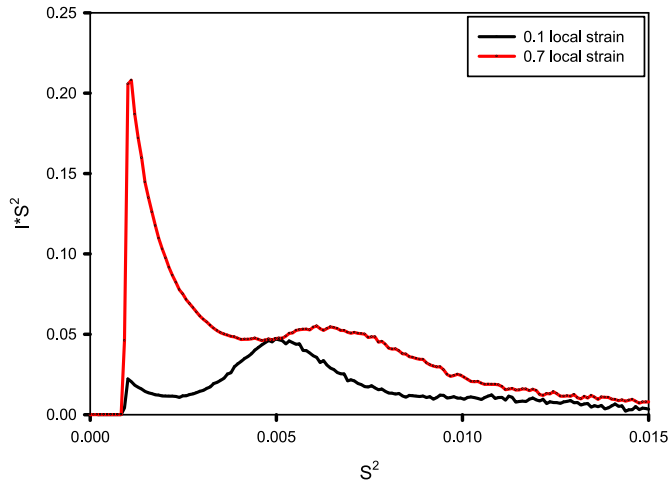

Fig. 13. Exemplary Θ scans perpendicular to tensile direction of SAXS images for HDPE+1% G deformed to 0.1 and 0.7 of local strain presented in Guinier representation of $I*S^2$ vs. S^2. *S* is the scattering vector equal to $sin(2\Theta)/\lambda$ where Θ is the scattering angle and λ is the x-ray wavelength while I is the intensity of scattering.

In Fig. 14a (HDPE + G) and 14b (HDPE + rGO) a series of SAXS patterns for increasing local deformation for HDPE nanocomposites are presented.

The inner fragment of SAXS patterns indicate an intense cavitation in all nanocomposites studied and also in plain HDPE. In the plain HDPE cavitation is absent at local strain of 10%, i.e. before reaching the mechanical yield, however, in nanocomposites at higher concentration of graphene and rGO cavitation is detected even before the yield (increased x-ray scattering seen in SAXS images around and close to the beam stop for 10% of local strain). As the local strain increases the cavitation intensity strongly increases.

The sizes of cavities are above the "long period" values because the x-ray scattering from voids falls at lower angles than for "long period". One of the ways to determine their sizes is using Gunier approach. According to Guinier approximation [76], if N groups of voids with different sizes exist in material, the intensity of scattering, *I*, is described by equation (6):

$$I = K \sum_{i=1}^{N} v_i \exp\left(-\frac{h^2 R_i^2}{3}\right) \tag{6}$$

where *K* is a constant, $v_i$is the volume of voids in the *i*th group, $R_i$is the radius of gyration, and *h* is the scattering vector. We used earlier that approach for the determination of fraction of cavities in various systems [62,77]. With our SAXS installation the upper resolution is approximately 80 nm, limiting by the beam stop and beam divergence. Also here the application of the Guinier approach gives us the fractions of cavity pores in the range from 25 to 80 nm with the majority of cavitation pores closer to 80 nm than to 25 nm. However, there are also many larger pores that scatter light (370–800 nm) and make the material whitened. There is evident lack of cavities smaller than 25 nm. Such cavities are created during drawing, however, they close themselves at early stages very probably due to the surface tension. The estimation of closing pressure is based on the formula in which the pressure is reciprocally proportional to the radius of a pore [22]:

$$p = -2\tau_s/r \tag{7}$$

where τ_s is the surface tension and r is the size of a pore. For HDPE the surface tension at room temperature can be assumed at the level of 35 mN/m [78] while the stress during plastic flow of HDPE is at the level of 10 MPa (see Fig. 6a and b). The pressure exerted by tensile stress is 10 MPa/3 = 3.3 MPa. Hence the radius of stable pores should be larger than

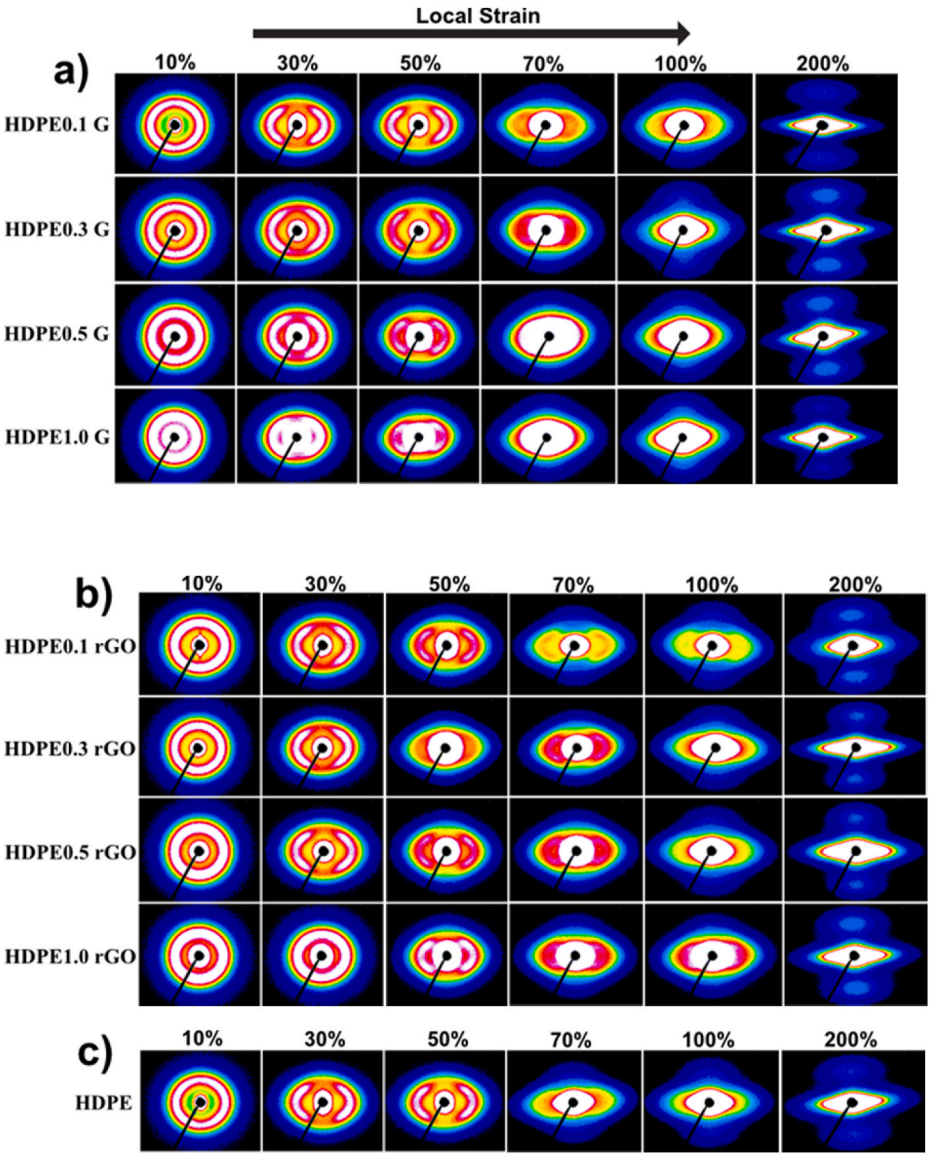

Fig. 14. SAXS patterns for HDPE + graphene nanocomposites (a), HDPE + rGO nanocomposites (b) and plain HDPE (c) at indicated local strains are shown. Deformation direction vertical.

2*(35 mN/m)/3.3 MPa ≈ 21 nm. In fact smaller pores are not observed in in-situ SAXS experiments.

As the local strain is increased the cavities reorient and assume elongated shapes. It is seen in SAXS patterns in Fig. 12 as rhomboidal form in their centers.

4. Conclusions

HDPE polymer tightly embraces graphene nanoplatelets as it follows from TEM observation of ultrathin section of graphene and rGO nanocomposites. Graphene platelets nucleate crystallization of HDPE while reduced graphene oxide does not. The onset of nonisothermal crystallization is the 2–3 deg higher for HDPE + graphene nanocomposites which results in a fraction of thicker HDPE crystals, becoming even thicker for higher concentration of graphene. A slight increase in the yield stress in graphene nanocomposites is observed. No such effect is seen for rGO nanocomposites.

Plastic flow during tensile drawing is subjected to fluctuation: the zone of intense deformation in the neck is migrating from one end of a neck to another which causes fluctuations on the stress. The reason is the interplay of strengthening by orientation and softening by heat generated during plastic deformation. Such effects disappear when the drawing is performed in more isothermal conditions.

Fracture in Izod impact strength measurement of nanocomposites occurs by debonding of HDPE from graphene or rGO and by fast radial spreading of fracture from debonded particles. The radial zones are freely spreading until impingement with neighbors when the travel of crack tip is slower, farther from the notch.

In tensile drawing of nanocomposites the debonding occurs even before the yielding is reached. The debonded nanoplateletes are the source of intense cavitation. The number of cavities in nanocomposites is higher for higher concentration of nanoplatelets. The sizes of cavitation pores are above 25 nm as it is judged from SAXS experiments. All smaller pores were healed by surface tension. In contrary, whitening of nanocomposites indicates that cavitational pores can reach the size of the light wavelength. Finally, there is only a small difference between graphene and rGO nanocomposites in the nucleation of crystallization of HDPE.

Declaration of competing interest

The authors declare that they have no known competing financial interests or personal relationships that could have appeared to influence the work reported in this paper.

Acknowledgements

The project was financed from funds of the National Science Centre on the basis of the decisions number DEC-2016/23/B/ST8/03509.

References

[1] S. Sahebian, S.M. Zebarjad, S.A. Sajjadi, Z. Sherafat, A. Lazzeri, Effect of both uncoated and coated calcium carbonate on fracture toughness of HDPE/CaCO3 nanocomposites, J. Appl. Polym. Sci. 104 (6) (2007) 3688–3694.
[2] N.C. Chen, L. Ma, T. Zhang, Investigation of nano-talc as a filling material and a reinforcing agent in high density polyethylene (HDPE), Rare Met. 25 (2006) 422–425.
[3] M. Pollanen, U. Pelz, M. Suvanto, T.T. Pakkanen, Effective method for dispersing SiO2 nanoparticles into polyethylene, J. Appl. Polym. Sci. 116 (2) (2010) 1218–1225.
[4] J.H. Yang, C.Y. Wang, K. Wang, Q. Zhang, F. Chen, R.N. Du, Q. Fu, Direct formation of nanohybrid shish-kebab in the injection molded bar of polyethylene/multiwalled carbon nanotubes composite, Macromolecules 42 (18) (2009) 7016–7023.
[5] J.F. Vega, J. Martinez-Salazar, M. Trujillo, M.L. Arnal, A.J. Muller, S. Bredeau, P. Dubois, Rheology, processing, tensile properties, and crystallization of polyethylene/carbon nanotube nanocomposites, Macromolecules 42 (13) (2009) 4719–4727.
[6] C. Lotti, C.S. Isaac, M.C. Branciforti, R.M.V. Alves, S. Liberman, R.E.S. Bretas, Rheological, mechanical and transport properties of blown films of high density polyethylene nanocomposites, Eur. Polym. J. 44 (5) (2008) 1346–1357.
[7] S.C. Tjong, S.P. Bao, Fracture toughness of high density polyethylene/SEBS-g-MA/montmorillonite nanocomposites, Compos. Sci. Technol. 67 (2) (2007) 314–323.
[8] T.C. Mokhena, A.S. Luyt, Investigation of polyethylene/sisal whiskers nanocomposites prepared under different conditions, Polym. Compos. 35 (11) (2014) 2221–2233.
[9] V. Tan, W. Abdallah, M.R. Kamal, The effect of cellulose nanocrystals (CNC) on isothermal crystallization kinetics of LLDPE and HDPE, Int. Polym. Process. 33 (3) (2018) 371–380.
[10] S.C. Tjong, G.D. Liang, Electrical Behavior of High Density polyethylene/ZnO Nano-Composites, e-Polymers, 2007, p. 10.
[11] S.C. Li, Y.N. Li, Mechanical and antibacterial properties of modified nano-ZnO/high-density polyethylene composite films with a low doped content of nano-ZnO, J. Appl. Polym. Sci. 116 (5) (2010) 2965–2969.
[12] P. Fei, B.H. Fei, Y. Yu, H.G. Xiong, J. Tan, Thermal properties and crystallization behavior of bamboo fiber/high-density polyethylene composites: nano-TiO2 effects, J. Appl. Polym. Sci. 131 (3) (2014) 10.
[13] M.J. Shirkavand, H. Azizi, I. Ghasemi, M. Karabi, Effect of molecular structure parameters on crystallinity and environmental stress cracking resistance of high-density polyethylene/TiO2 nanocomposites, Adv. Polym. Technol. 37 (3) (2018) 8.
[14] R. Asmatulu, W.S. Khan, R.J. Reddy, M. Ceylan, Synthesis and analysis of injection-molded nanocomposites of recycled high-density polyethylene incorporated with graphene nanoflakes, Polym. Compos. 36 (9) (2015) 1565–1573.
[15] X. Jiang, L.T. Drzal, Improving electrical conductivity and mechanical properties of high density polyethylene through incorporation of paraffin wax coated exfoliated graphene nanoplatelets and multi-wall carbon nano-tubes, Compos. Appl. Sci. Manuf. 42 (11) (2011) 1840–1849.
[16] J.H. Du, L. Zhao, Y. Zeng, L.L. Zhang, F. Li, P.F. Liu, C. Liu, Comparison of electrical properties between multi-walled carbon nanotube and graphene nanosheet/high density polyethylene composites with a segregated network structure, Carbon 49 (4) (2011) 1094–1100.
[17] C.Y. Wan, B.Q. Chen, Reinforcement and interphase of polymer/graphene oxide nanocomposites, J. Mater. Chem. 22 (8) (2012) 3637–3646.
[18] X. Jiang, L.T. Drzal, Multifunctional high-density polyethylene nanocomposites produced by incorporation of exfoliated graphene nanoplatelets 2: crystallization, thermal and electrical properties, Polym, Compos 33 (4) (2012) 636–642.
[19] T. Evgin, A. Turgut, G. Hamaoui, Z. Spitalsky, N. Horny, M. Micusik, M. Chirtoc, M. Sarikanat, M. Omastova, Size effects of graphene nanoplatelets on the properties of high-density polyethylene nanocomposites: morphological, thermal, electrical, and mechanical characterization, Beilstein J. Nanotechnol. 11 (2020) 167–179.
[20] Y.G. Li, T.C. Duan, G.B. Yao, Y.J. Tang, W.J. Miao, Z.B. Wang, Structural evolution of stretch deformed HDPE/RGO nanocomposites: an in-situ synchrotron SAXS and WAXD study, Compos. Sci. Technol. 183 (2019) 9.
[21] Z. Seibers, M. Orr, G.S. Collier, A. Henriquez, M. Gabel, M.L. Shofner, V. La Saponara, J. Reynolds, Chemically functionalized reduced graphene oxide as additives in polyethylene composites for space applications, Polym. Eng. Sci. 60 (1) (2020) 86–94.
[22] A. Pawlak, A. Galeski, Plastic deformation of crystalline polymers: the role of cavitation and crystal plasticity, Macromolecules 38 (23) (2005) 9688–9697.
[23] A. Pawlak, A. Galeski, A. Rozanski, Cavitation during deformation of semicrystalline polymers, Prog. Polym. Sci. 39 (5) (2014) 921–958.
[24] A. Rozanski, A. Galeski, M. Debowska, Initiation of cavitation of polypropylene during tensile drawing, Macromolecules 44 (1) (2011) 20–28.
[25] A. Rozanski, A. Galeski, Plastic yielding of semicrystalline polymers affected by amorphous phase, Int. J. Plast. 41 (2013) 14–29.
[26] A. Rozanski, A. Krajenta, R. Idczak, A. Galeski, Physical state of the amorphous phase of polypropylene-influence on free volume and cavitation phenomenon, J. Polym. Sci. B Polym. Phys. 54 (5) (2016) 531–543.
[27] B. Xiong, O. Lame, J.M. Chenal, C. Rochas, R. Seguela, G. Vigier, In-situ SAXS study and modeling of the cavitation/crystal-shear competition in semi-crystalline polymers: influence of temperature and microstructure in polyethylene, Polymer 54 (20) (2013) 5408–5418.
[28] Y. Lu, Y.F. Men, Cavitation-induced stress whitening in semi-crystalline polymers, Macromol. Mater. Eng. 303 (11) (2018) 31.
[29] A. Galeski, A. Argon, R.E. Cohen, Changes in the morphology of bulk spherulitic nylon 6 due to plastic deformation, Macromolecules 21 (9) (1988) 2761–2770.
[30] A. Rozanski, A. Galeski, Crystalline lamellae fragmentation during drawing of polypropylene, Macromolecules 48 (15) (2015) 5310–5322.
[31] A. Galeski, A.S. Argon, R.E. Cohen, Morphology of bulk nylon-6 subjected to plane-strain compression, Macromolecules 24 (13) (1991) 3953–3961.
[32] S. Kapur, K. Matsushige, A. Galeski, E. Baer, The effect of pressure and environment on the fracture and yield of polymers, in: D.N.R. Taplin (Ed.), Advances in Research on the Strength and Fracture of Materials, Pergamon Press, New York, 1978, pp. 1079–1086.
[33] Y. Lu, Y.T. Wang, R. Chen, J.Y. Zhao, Z.Y. Jiang, Y.F. Men, Cavitation in lsotactic polypropylene at large strains during tensile deformation at elevated temperatures, Macromolecules 48 (16) (2015) 5799–5806.
[34] Y. Lu, D. Lyu, Y.J. Tang, L. Qian, Y.N. Qin, M.Y. Xiang, Y.F. Men, Effect of alpha(c)-relaxation on the large strain cavitation in polyethylene, Polymer 210 (2020) 13.
[35] J. Morawiec, A. Pawlak, M. Slouf, A. Galeski, E. Piorkowska, N. Krasnikowa, Preparation and properties of compatibilized LDPE/organo-modified montmorillonite nanocomposites, Eur. Polym. J. 41 (5) (2005) 1115–1122.
[36] D. Liu, A.M. Pourrahimi, R.T. Olsson, M.S. Hedenqvist, U.W. Gedde, Influence of nanoparticle surface treatment on particle dispersion and interfacial adhesion in low-density polyethylene/aluminium oxide nanocomposites, Eur. Polym. J. 66 (2015) 67–77.
[37] M. Perchacz, A. Rozanski, H. Kargarzadeh, A. Galeski, Cavitation in high density polyethylene/Al2O3 nanocomposites, Compos. Sci. Technol. 199 (2020) 13.
[38] A. Sudar, J. Moczo, G. Voros, B. Pukanszky, The mechanism and kinetics of void formation and growth in particulate filled PE composites, Express Polym. Lett. 1 (11) (2007) 763–772.
[39] B. Pukanszky, M. Vanes, F.H.J. Maurer, G. Voros, Micromechanical deformations in particulate filled thermoplastics-volume strain measurements, J. Mater. Sci. 29 (9) (1994) 2350–2358.
[40] B.V. Pukanszky, G, Mechanism of interfacial interactions in particulate filled composites, Compos. Interfac. 1 (5) (1993) 411–427.
[41] D. Eiras, L.A. Pessan, Mechanical properties of polypropylene/calcium carbonate nanocomposites, Mater. Res.-Ibero-am. J. Mater. 12 (4) (2009) 517–522.
[42] A.V. Zhuk, N.N. Knunyants, V.G. Oshmyan, V.A. Topolkaraev, A.A. Berlin, Debonding microprocesses and interfacial strength in particle-filled polymer materials, J. Mater. Sci. 28 (17) (1993) 4595–4606.
[43] B. Lee, S. Onbulak, Y.W. Xu, V. Topolkaraev, R. McEneany, F. Bates, M. Hillmyer, Investigation of micromechanical behavior and voiding of polyethylene terephthalate/polyethylene-stat-methyl acrylate blends during tensile deformation, Ind. Eng. Chem. Res. 58 (16) (2019) 6402–6412.
[44] D. Liu, L.K.H. Pallon, A.M. Pourrahimi, P. Zhang, A. Diaz, M. Holler, K. Schneider, R.T. Olsson, M.S. Hedenqvist, S. Yu, U.W. Gedde, Cavitation in strained polyethylene/aluminium oxide nanocomposites, Eur. Polym. J. 87 (2017) 255–265.
[45] J. Cayer-Barrioz, L. Ferry, D. Frihi, K. Cavalier, R. Seguela, G. Vigier, Microstructure and mechanical behavior of polyamide 66-precipitated calcium carbonate composites: influence of the particle surface treatment, J. Appl. Polym. Sci. 100 (2) (2006) 989–999.
[46] S. Lee, S. Ryu, Theoretical study of the effective modulus of a composite considering the orientation distribution of the fillers and the interfacial damage, Eur. J. Mech. Solid. 72 (2018) 79–87.
[47] R.B. Ladani, M. Bhasin, S.Y. Wu, A.R. Ravindran, K. Ghorbani, J. Zhang, A. J. Kinloch, A.P. Mouritz, C.H. Wang, Fracture and fatigue behaviour of epoxy nanocomposites containing 1-D and 2-D nanoscale carbon fillers, Eng. Fract. Mech. 203 (2018) 102–114.
[48] G.H. Michler, H.-H.K.-B. von Schmeling, The physics and micro-mechanics of nano-voids and nano-particles in polymer combinations, Polymer 54 (13) (2013) 3131–3144.
[49] N. Lepot, M.K. Van Bael, H. Van den Rul, R. Peeters, J. Mullens, D. Franco, Nanoparticles of gamma-Al2O3 as perspective fillers of thermoplastic polymers improving their barrier properties, Polimery 51 (9) (2006) 662–664.
[50] S. Ouchiar, G. Stoclet, C. Cabaret, A. Addad, V. Gloaguen, Effect of biaxial stretching on thermomechanical properties of polylactide based nanocomposites, Polymer 99 (2016) 358–367.
[51] N. Lepot, M.K. Van Bael, H. Van den Rul, J. D'Haen, R. Peeters, D. Franco, J. Mullens, Influence of incorporation of ZnO nanoparticles and biaxial orientation on mechanical and oxygen barrier properties of polypropylene films for food packaging applications, J. Appl. Polym. Sci. 120 (3) (2011) 1616–1623.
[52] A. Rozanski, A. Galeski, Modification of amorphous phase of semicrystalline polymers, Polimery 57 (6) (2012) 433–440.

[53] L.A. Utracki, M.R. Kamal, Clay-containing polymeric nanocomposites, Arabian J. Sci. Eng. 27 (1C) (2002) 43–67.
[54] A. Pawlak, J. Morawiec, E. Piorkowska, A. Galeski, Polypropylene nanocomposites - preparation and properties, in: W. Lojkowski, J.R. Blizzard (Eds.), Interfacial Effects and Novel Properties of Nanomaterials, Trans Tech Publications Ltd, Zurich-Uetikon, 2003, pp. 335–338.
[55] C.Y. Ren, Z.Y. Jiang, X.H. Du, Y.F. Men, T. Tang, Microstructure and deformation behavior of polyethylene/montmorillonite nanocomposites with strong interfacial interaction, J. Phys. Chem. B 113 (43) (2009) 14118–14127.
[56] L. Laiarinandrasana, O. Klinkova, F. Nguyen, H. Proudhon, T.F. Morgeneyer, W. Ludwig, Three dimensional quantification of anisotropic void evolution in deformed semi-crystalline polyamide 6, Int. J. Plast. 83 (2016) 19–36.
[57] F. Addiego, J. Di Martino, D. Ruch, A. Dahoun, O. Godard, P. Lipnik, J.J. Biebuyck, Cavitation in unfilled and nano-CaCo(3) filled HDPE subjected to tensile test: revelation, localization, and quantification, Polym. Eng. Sci. 50 (2) (2010) 278–289.
[58] F. Addiego, A. Dahoun, C. G'Sell, J.M. Hiver, Characterization of volume strain at large deformation under uniaxial tension in high-density polyethylene, Polymer 47 (12) (2006) 4387–4399.
[59] A. Pawlak, Cavitation during tensile deformation of high-density polyethylene, Polymer 48 (5) (2007) 1397–1409.
[60] S. Humbert, O. Lame, J.M. Chenal, C. Rochas, G. Vigier, New insight on initiation of cavitation in semicrystalline polymers: in-situ SAXS measurements, Macromolecules 43 (17) (2010) 7212–7221.
[61] A. Pawlak, A. Galeski, Cavitation during tensile drawing of annealed high density polyethylene, Polymer 51 (24) (2010) 5771–5779.
[62] A. Pawlak, A. Galeski, Cavitation during tensile deformation of polypropylene, Macromolecules 41 (8) (2008) 2839–2851.
[63] B. Wunderlich, G. Czornyj, Study of equilibrium melting of polyethylene, Macromolecules 10 (5) (1977) 906–913.
[64] G. Porod, General theory, in: O. Glater, O. Kratky (Eds.), Small Angle X-Ray Scattering, Academic Press, London, 1982, pp. 17–52.
[65] C.J. Shearer, A.D. Slattery, A.J. Stapleton, J.G. Shapter, C.T. Gibson, Accurate thickness measurement of graphene, Nanotechnology 27 (12) (2016) 125704.
[66] A. Bondi, van der Waals volumes and radii, J. Phys. Chem. 68 (3) (1964) 441–451.
[67] J.D. Hoffman, G.T. Davis, J.I. Lauritzen, The rate of crystallization of linear polymers with chain folding, in: N.B. Hannay (Ed.), Teatise on Solid State Chemistry, Plenum Press New York, 1976, pp. 497–614.
[68] B. Wunderlich, Macromolecular Physics Volume 1, Crystal Structure, Morphology, Defects, Academic Press, New York, 1973.
[69] M. Iijima, G. Strobl, Isothermal crystallization and melting of isotactic polypropylene analyzed by time- and temperature-dependent small-angle X-ray scattering experiments, Macromolecules 33 (14) (2000) 5204–5214.
[70] F.G. Hamad, R.H. Colby, S.T. Milner, Lifetime of flow-induced precursors in isotactic polypropylene, Macromolecules 48 (19) (2015) 7286–7299.
[71] J. Xu, B. Heck, H.-M. Ye, J. Jiang, Y.-R. Tang, J. Liu, B.-H. Guo, R. Reiter, D.-S. Zhou, G. Reiter, Stabilization of nuclei of lamellar polymer crystals: insights from a comparison of the hoffman–weeks line with the crystallization line, Macromolecules 49 (6) (2016) 2206–2215.
[72] M. Psarski, E. Piorkowska, A. Galeski, Crystallization of polyethylene from melt with lowered chain entanglements, Macromolecules 33 (3) (2000) 916–932.
[73] B. Crist, F.M. Mirabella, Crystal thickness distributions from melting homopolymers or random copolymers, J. Polym. Sci. B Polym. Phys. 37 (1999) 3131–3140.
[74] J.D. Hoffman, Role of reptation in the rate of crystallization of polyethylene fractions from the melt, Polymer 23 (5) (1982) 656–670.
[75] B. Wunderlich, G. Czornyj, A study of equilibrium melting of polyethylene, Macromolecules 10 (5) (1977) 906–913.
[76] Andre Guinier, Gerard Fournet, Small-Angle Scattering of X-Rays, John Wiley & Sons, New York, 1955.
[77] H. Kargarzadeh, A. Galeski, A. Pawlak, PBAT green composites: effects of kraft lignin particles on the morphological, thermal, crystalline, macro and micromechanical properties, Polymer 203 (2020) 122748.
[78] S. Wu, Surface and interfacial tensions of polymer melts: I. Polyethylene, polyisobutylene, and polyvinyl acetate, J. Colloid Interface Sci. 31 (1969) 153–161.